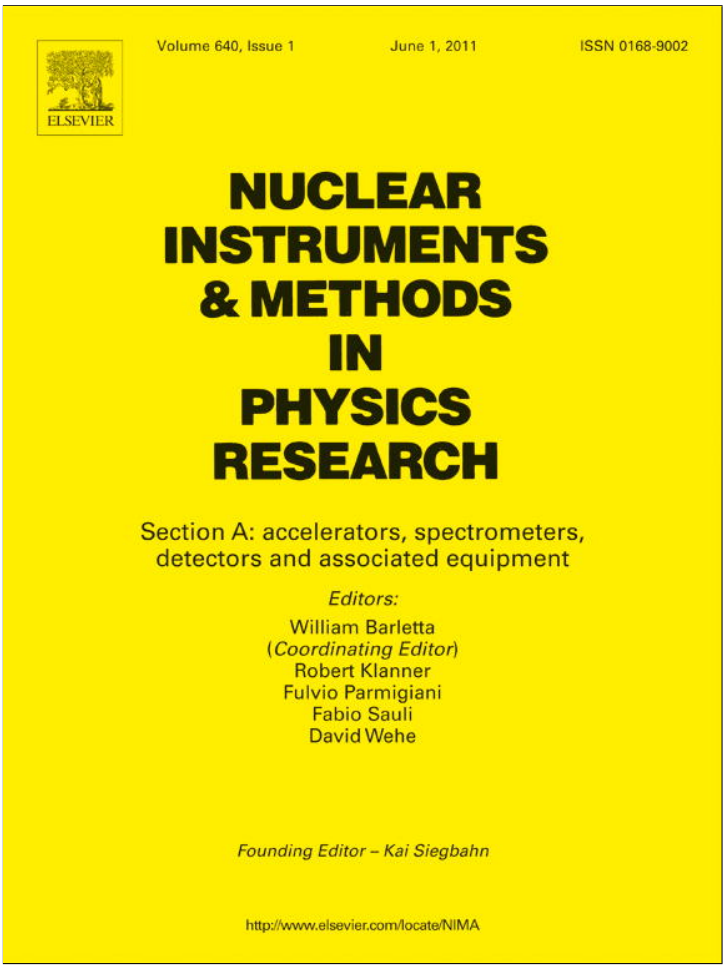

Nuclear Instruments and Methods in Physics Research A 640 (2011) 192–199

Contents lists available at ScienceDirect

Nuclear Instruments and Methods in Physics Research A

journal homepage: www.elsevier.com/locate/nima

Parameters affecting image quality with Time-Resolved Optical Integrative Neutron (TRION) detector

I. Mor [a,*], D. Vartsky [a], G. Feldman [a], V. Dangendorf [b], D. Bar [a], M.B. Goldberg [a], K. Tittelmeier [b], B. Bromberger [b], M. Weierganz [b], M. Brandis [a]

[a] Soreq NRC, Yavne 81800, Israel
[b] Physikalisch-Technische Bundesanstalt (PTB), 38116 Braunschweig, Germany

ARTICLE INFO

Article history:
Received 13 December 2010
Received in revised form
2 March 2011
Accepted 2 March 2011
Available online 9 March 2011

Keywords:
Fast-neutrons
Point-spread function
Neutron radiography
Spatial-resolution
Fiber scintillator

ABSTRACT

We have investigated by simulations and experimentally the parameters that affect image quality (contrast and spatial-resolution) of the fast neutron TRION detector. A scintillating fiber screen with 0.5×0.5 mm^2 square fibers, few centimeters thick, provides superior spatial-resolution to that of a slab scintillator of the same thickness. A detailed calculation of the neutron interaction processes that influence the point-spread function (PSF) in the scintillating screen has been performed using the GEANT 3.21 code. The calculations showed that neutron scattering within the screen accounts for a significant loss of image contrast. The factors that limit the spatial-resolution of the image are the cross-sectional scintillating-fiber dimensions within the screen and the spatial response of the image-intensifier. A deconvolution method has been applied for restoring the contrast and the spatial-resolution of the fast neutron image.

1. Introduction

Detection of explosives concealed in air-cargo or passenger-baggage presents a considerable challenge that has not been fully met by currently deployed X-ray and gamma-ray inspection systems. These systems provide only limited information about the objects contained, such as their shape and density, while detection capabilities of contraband rely heavily on human operator skill. Furthermore, only very limited differentiation amongst elements in the low atomic-number (Z) range can be achieved. The sole X-ray based explosives detection technique capable of automatic detection utilizes coherent X-ray scattering [1]. However, its penetration through items that are substantially more massive than carry-on baggage is severely limited by the low energy of the relevant X-rays (<100 keV).

Over the years, various neutron-based imaging methods were considered for use in screening baggage and air-cargo [2–12]. One of the neutron-based methods proven of revealing the elemental composition of materials is Fast-Neutron Resonance Radiography (FNRR). This method is based on measurement of the neutron transmission through the inspected object as function of neutron energy. The energy spectrum of the transmitted neutrons is modified according to cross-section fluctuations ("peaks" and "dips") exhibited by light elements in the 1–10 MeV energy range. It offers determination of the elemental density distribution of C, N, O and possibly H within closed shipping containers or boxes of mediums size, e.g. air-cargo or light trucks. Thus, FNRR is one of the most promising methods for fully automatic detection and identification of explosives concealed in passenger luggage and air-cargo. For a review of various FNRR methods see Ref. [13].

The FNRR method that utilizes neutron Time-of-Flight (TOF) techniques for determining the transmitted neutron spectrum is called Pulsed Fast Neutron Transmission Spectroscopy (PFNTS). The PFNTS method was proposed and first studied by Oregon University as of 1985 [2–3,14–18] and subsequently refined by Tensor-Technology Inc. [4,19–23] culminating in series of blind tests conducted during the late 1990s by the US Federal Aviation Administration (FAA) [4]. The results of these tests demonstrated that PFNTS constitutes a powerful detection method for detecting bulk explosives. However, the pixel size defined by these detectors (several centimeters) imposed an intrinsic limitation on the spatial-resolution, which prohibited reliable detection of objects smaller and thinner than, typically, 2–3 cm. Thus, in 1999, the National Materials Advisory Board Panel [4], advised against constructing an operational airport prototype, since neither a compact, suitable neutron source was available at that time, nor was the detector spatial-resolution adequate for reliable detection of thin-sheet explosives. Nevertheless, the panel did conclude that a mature inspection system of this type, being completely automatic, would represent a significant improvement over systems available then (and now).

In order to respond to the above challenge, a new kind of PFNTS detectors were developed in recent years—Time-Resolved Integrative Optical Neutron (TRION) detector. These detectors are capable of

* Corresponding author. Tel.: +972 54 4625944.
E-mail address: ilanmor@yahoo.com (I. Mor).

0168-9002/$ - see front matter © 2011 Elsevier B.V. All rights reserved.
doi:10.1016/j.nima.2011.03.007

providing mm-size spatial-resolution and good TOF spectroscopy (few ns, which translates to several hundred keV) per pixel as well as the ability to operate at high neutron fluxes ($\geq 10^6$ n/(s × cm^2)). The following chapters present a theoretical and experimental evaluation of the imaging properties of two generations of TRION systems.

2. TRION detectors

The concept was first proposed in 2004 [24] and jointly developed at Soreq NRC and PTB [25–27]. Here we shall give only a brief outline of each TRION generation. A detailed description of the two TRION generations can be found in Ref. [25].

TRION is a fast-neutron imaging device based on a time-gated optical readout. The detector is designed to detect fast-neutron pulses produced, for example, in the ^{9}Be(d,n) reaction using a pulsed (~1–2 ns bursts, 1–2 MHz repetition rate) deuteron beam. After a specific Time-of-Flight (TOF) that depends on the neutron energy and the distance between source and detector, the fast-neutrons impinge on the plastic scintillating fiber screen, causing the emission of light from the screen surface, mainly via recoil protons. The light is reflected by a front-coated bending mirror (98% reflectivity), positioned at an angle of 45° relative to the neutron beam direction, towards a large aperture 120 mm F#0.95 lens positioned at a distance of 750 mm from the scintillating screen and subsequently focused on an image-intensifier. The latter not only amplifies the light intensity but, more importantly, acts as an electronic shutter that is opened for a gate period of Δt (as short as 4–6 ns) at a fixed, pre-selected TOF relative to each beam burst. Repetition rate for the beam pulses was up to 2 MHz and images were integrated by a cooled CCD camera over many beam bursts, with acquisition times ranging from tens to several hundreds of seconds.

All system components are mounted in a light-tight enclosure.

With TRION Generation 1 (Gen. 1), TOF multiple energy imaging is performed sequentially, i.e., for each specific neutron energy the intensifier is triggered to capture the corresponding TOF interval, per each accelerator burst. This procedure is time consuming and inefficient in its use of the broad-energy neutron spectrum. Thus, in order to progress towards a real-time operational system, it is necessary to acquire images for several TOF frames (or corresponding pre-selected energy regions) simultaneously. This can be achieved by employing several ns-triggered intensified CCD cameras, such that each camera acquires a transmission image corresponding to a different energy region. This is the principle of operation of TRION Gen. 2. In TRION Gen. 2 the image transferred by the large aperture 120 mm F#0.95 lens is first amplified by an un-gated custom-made image-intensifier with a fast phosphor. This fast phosphor screen is viewed by four gated CCD cameras. In TRION Gen. 2, the CCD cameras have coarser resolution (512 × 512 pixels, 20 × 20 micron^2 pixel size) compared to that of Gen. 1 (1536 × 1024 pixels, 9 × 9 μm^2 pixel size). Figs. 1 and 2 show images of TRION Gen. 1 and 2, respectively. This reduction in spatial-resolution is acceptable as this application does not require spatial-resolution better than 1 mm.

3. Spatial-resolution and contrast of TRION detectors

Each of TRION's components may influence the spatial-resolution obtained with the detector. In this section, we will attempt to

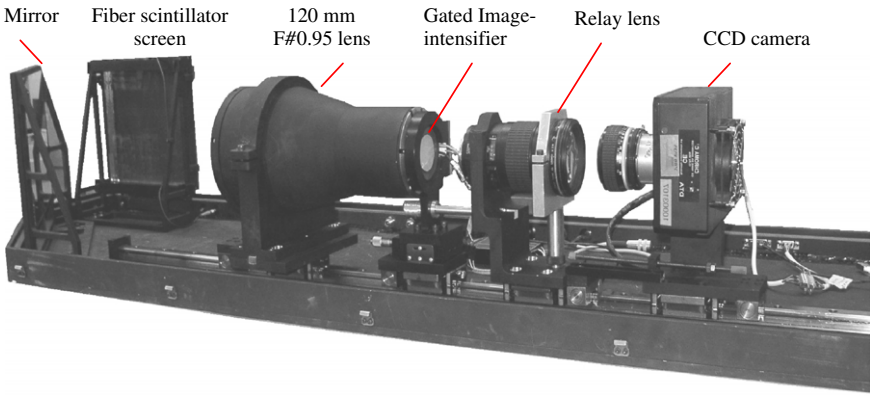

Fig. 1. TRION Gen. 1.

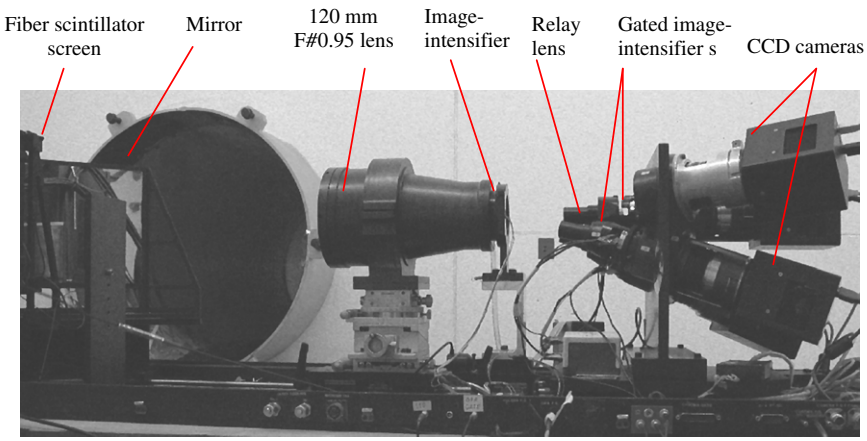

Fig. 2. TRION Gen. 2.

separate the different contributors to image quality of the system by measuring its influence on the Contrast Transfer Function (CTF). CTF provides a measure of how well the detection system reproduces the real contrast of the radiographed object at different spatial frequencies.

The CTF of pure optics (excluding neutron related influence) was determined using a bar-patterned semi-transparent mask containing a series of slits with increasing spatial-frequency, as illustrated in Fig. 3a. An electro-luminescent screen coupled to a polyethylene light diffuser was used as a uniform light source to transmission-illuminate the mask. The CTF of the neutron image was determined using a steel or tungsten mask of identical dimensions, seen in Fig. 3b.

CTF is defined as the following ratio and is measured as function of spatial-frequency, commonly described in units of line-pairs/mm (lp/mm):

$$CTF(\%) = \frac{[(C_{dk}-C_{bt})/(C_{dk}+C_{bt})]_{obs}}{[(C_{dk}-C_{bt})/(C_{dk}+C_{bt})]_{\exp}} \times 100 \quad (1)$$

where C_{dk} and C_{bt} are the gray-level values of dark and bright regions of the picture, respectively, "*obs*" and "*exp*" refer to observed and expected values, respectively.

Using the CTF function we shall analyze the influence of the following system components on image quality:

- The scintillating screen
- The optical system
- The electro-optical components
- Overall spatial-resolution

3.1. Scintillating screen

3.1.1. Slab screen vs. fiber screen

In order to obtain detection efficiency of 5–15% for fast-neutrons (1–10 MeV), the thickness of the scintillating screen must be in the range of 10–30 mm. We have investigated the effect of screen thickness on CTF using plain slab scintillators of different thicknesses and compared them to that of a scintillating fiber screen.

Fig. 4 shows a 7.5 MeV neutron image of the steel mask obtained using 10 mm-thick scintillating fiber screen (left) and 10 mm-thick plain slab scintillator (right). The fiber screen, employed at the early stages of TRION Gen. 1, was manufactured by Saint-Gobain. It is consisted of 0.25×0.25 mm^2 polystyrene scintillating fibers. Each fiber is coated with white paint (Extra-Mural Absorber, EMA) to prevent light cross-talk. The plain slab screen was manufactured by EL-JEN from polyvinyltoluene (EJ-200).

Visual judgment already suggests that the image obtained with the scintillating fiber screen has a significantly better spatial-resolution.

Quantitative evidence is provided in Fig. 5, showing CTF curves for 3, 10 and 20 mm-thick slab scintillators and for the above mentioned 10 mm-thick fiber screen. As can be observed, the CTFs obtained with slabs deteriorate fast with screen thickness. The CTF of the 10 mm-thick fiber scintillator is superior even to a 3 mm-thick slab. This result is to be expected due to the short Depth-of-Field (DOF) range of our high aperture lens. The thinner the slab, the smaller the optical blurring, therefore the better the spatial-resolution, at the expense of detection efficiency. Obviously the thick fiber screen, where the optical image is projected to its surface plane, provides the best resolution at the highest detection efficiency. For this reason, fiber scintillator screens are favorable, due to the fact that for a given fiber cross-sectional dimensions the fiber screen maintains spatial-resolution independent of the screen thickness.

For a limiting CTF value of 10%, the corresponding spatial-frequency value is 0.88, 0.72, 0.7 and 0.3 lp/mm for the 10 mm-thick fiber screen and for 3, 10 and 20 mm-thick slab screens, respectively.

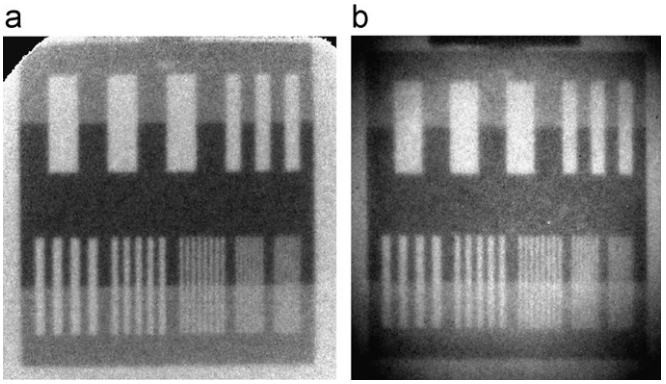

Fig. 4. Radiographic images of the steel patterned mask using (a) 10 mm scintillating fiber screen and (b) 10 mm plain slab scintillator.

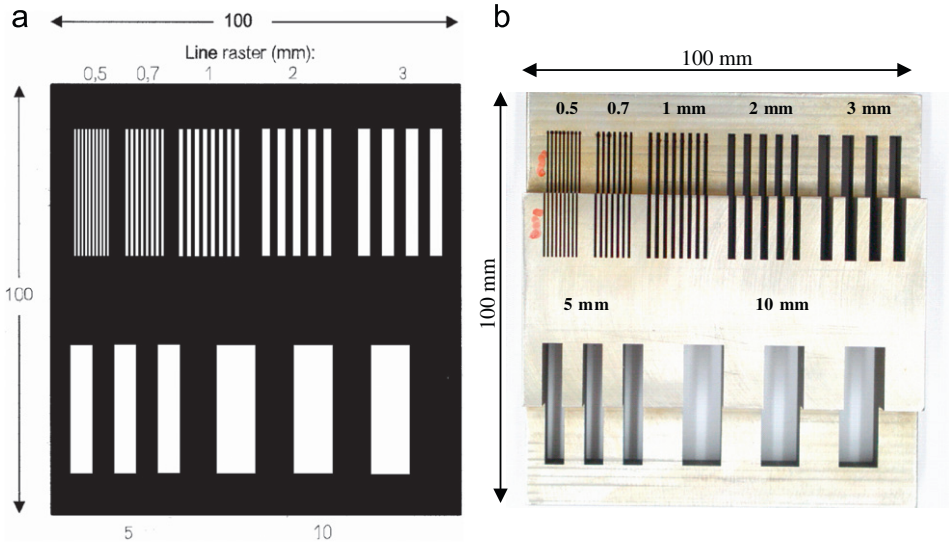

Fig. 3. Masks for CTF calculation: (left) optical bar-patterned mask, (right) steel mask. The numbers indicate the width of each line in the corresponding series below.

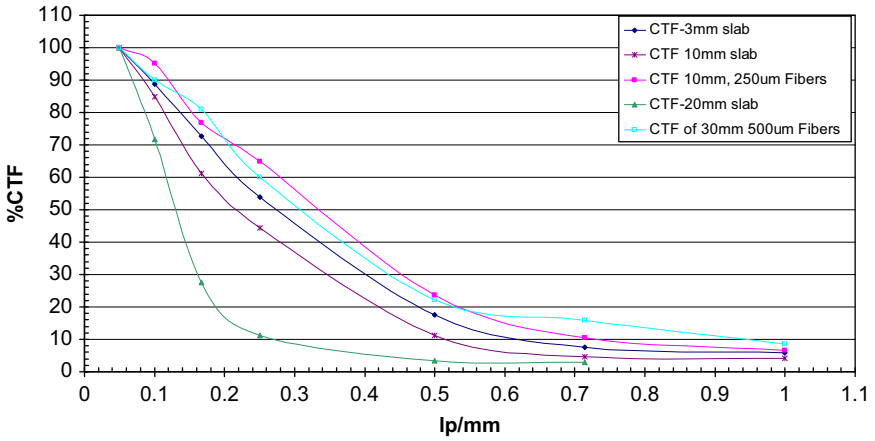

Fig. 5. CTF comparison between different scintillator screen types and thickness for 7.5 MeV neutrons.

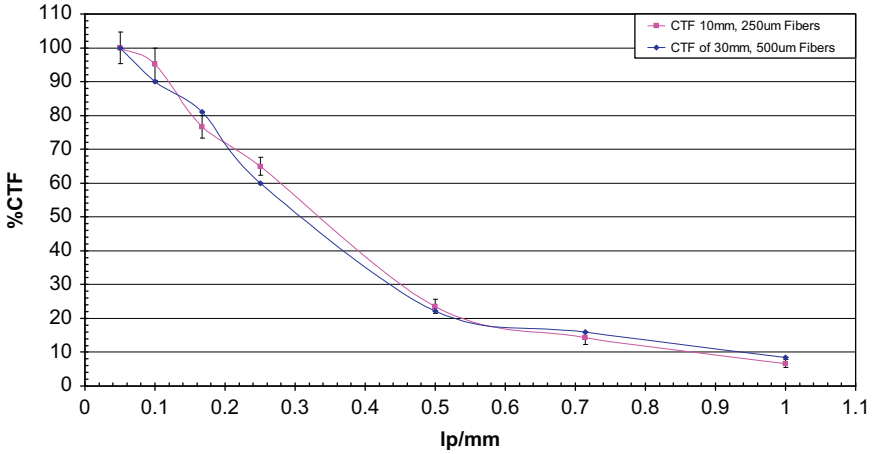

Fig. 6. CTF comparison between the two scintillating fiber screens with 7.5 MeV neutrons.

The Gen. 1 and Gen. 2 TRION systems are based on a $200 \times 200\ mm^2$ in area; 30 mm-thick fiber screen constructed from square $0.5 \times 0.5\ mm^2$ polystyrene scintillating fibers. Fig. 6 compares the CTF of this screen to that of the 10 mm-thick fiber screen described above using TRION Gen. 1. As can be observed, the threefold increase in thickness and coarser granulation do not introduce a significant deterioration in spatial-resolution.

The disadvantage of a scintillating fiber screen is that its light yield is lower than that of a slab screen. The reason for that may be attributed to light-output reduction due to the EMA [28], dead-layers and imperfections (broken fibers, incomplete or destroyed cladding), which reduce the effective scintillator screen area, and differences in scintillator composition. Nevertheless, the light yield can be increased by employing a reflecting mirror coupled to the front face of the fiber screen. Contrarily, in a slab scintillator this measure would result in a deterioration of spatial-resolution due to its dependence on the DOF effect. We have determined the net sensitive area of our scintillating fiber screen to be 60–70% of the total screen area. This loss of efficiency can in principle be compensated by increasing the thickness of the fiber screen, however, at some expense of the image quality due to additional neutron scattering within the volume of the screen. This effect is examined in the next section.

3.1.2. *Processes in the scintillating fiber screen*

The spatial-resolution of a scintillating fiber screen are affected by

- Range of the recoil proton generated by the incident neutron.
- The fiber cross-sectional dimensions.
- Multiple scattering of neutrons within the screen.
- Light cross-talk between fibers.

The fiber diameter determines the inherent image granularity, provided that the granularity introduced by the following system elements such as the image-intensifier and the CCD are of much smaller dimensions. The recoil proton generated by an incident fast neutron in the scintillator may cover a distance of several hundred microns (for example: a 3.75 MeV proton from a 7.5 MeV n,p collision) will travel 203 μm [29] before coming to rest within the scintillator and reach an average radial distance from the interaction point of ca 140 μm. Thus, the best achievable spatial-resolution is of the order of the average radial proton range within the scintillator for a given neutron energy. For neutron at energies of up to 14 MeV, a 500–700 μm fiber presents a suitable compromise between required spatial-resolution and the significantly increasing costs of fibers of smaller diameters.

Multiple neutron scattering, charged particle and light cross-talk between fibers will reduce the contrast. The cross-talk of light in our screens is prevented by coating the fibers with EMA; however, the neutron scattering within the screen cannot be suppressed.

In order to determine the effects of scattered neutrons and proton cross-talk, we calculated by Monte-Carlo the processes that take place in the fiber screen. A detailed calculation of the Point-Spread Function (PSF) in the scintillating screen has been performed using the GEANT 3.21 code [30]. The simulated setup

consisted of a $200 \times 200 \times 30\ mm^3$ fiber screen, irradiated at 5 different neutron energies (2, 4, 7.5, 10 and 14 MeV) by a mono-energetic infinitesimally thin pencil-beam of neutrons impinging upon the axis of the central fiber.

Fig. 7 (left) shows a schematic configuration of 9 fibers located at the center of the screen and a magnified view (right) of the central fiber ($0.5 \times 0.5\ mm^2$ polystyrene core, 20 μm-thick PolyMethyl-MethAcrylate (PMMA) cladding and 16 μm-thick EMA paint).

The simulation calculates the energy deposited by protons and amount of light created in the fibers, taking into account the non-linear light yield with proton energy. For tracking and tallying purposes, light created by knock-on protons created in the central fiber by incident neutrons is termed "primary signal". Light created outside the central fiber by protons escaping it is defined as "secondary signal" and signal created by neutrons scattered within the screen is defined as "tertiary signal".

Only the primary signal carries the correct radiographic information. The other signals will cause deterioration in spatial-resolution and loss of contrast.

For a given neutron energy, the secondary signal depends on the proton range relative to fiber dimensions and the tertiary signal depends on neutron beam dimensions and screen geometry. Since the tertiary protons are created by neutrons scattered within the screen, their contribution will vary with position across the screen

Fig. 8a shows the PSF obtained with 7.5 MeV neutrons and Fig. 8b the profile of primary, secondary and tertiary signal contributions to the PSF. As can be observed, the primary and secondary profiles are quite narrow; the Full Width Half Maximum (FWHM) of the total PSF (Fig. 8a) is 1 fiber, which corresponds to 0.572 mm (including cladding and EMA). However the tertiary signal distribution adds very broad wings to the PSF. The contribution of the tertiary signal over the entire detector area to the total signal amounts to 14%.

These wings in the PSF will cause a significant loss of contrast in transmission images as they add up to a significant baseline under the primary signal (see also Fig. 11).

Fig. 9 shows the dependence of PSF on incident neutron energy.

The central part of the PSF peak broadens with neutron energy due to increased range of the recoil protons. Fig. 10 shows the variation of normalized tertiary PSF with neutron energy. The tertiary light signal was normalized by the corresponding primary light signal for each energy. As can be seen, the wings from the tertiary signal are only slightly dependent on neutron energy.

In order to determine how this PSF affects the spatial-resolution and image contrast, we have calculated transmission image of 7.5 MeV neutrons through a steel plate 30 cm-thick with 9 holes, each 1 cm in diameter. The plate was positioned at a distance of 1 m from the fiber screen. The incident neutron beam was a collimated conic beam emitted from a spot 3 mm in diameter, at distance of 1200 cm from the screen face. This configuration simulates well our experimental conditions at the PTB cyclotron. Fig. 16a shows the mask that was used in this

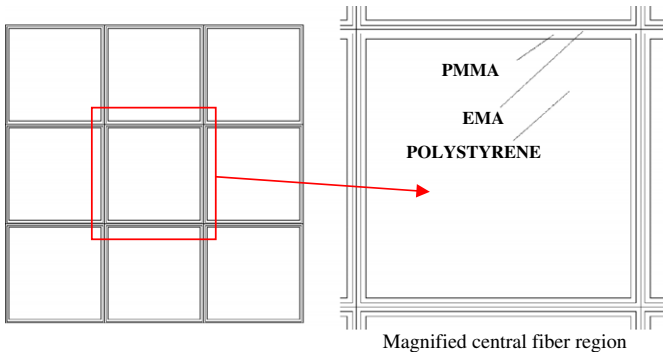

Fig. 7. Schematic of 9-fiber array (left) and magnified view of central fiber.

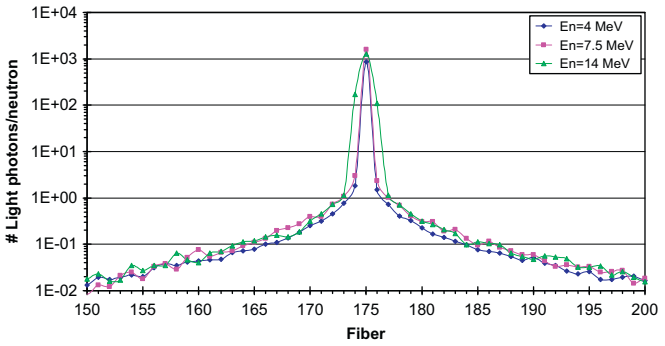

Fig. 9. Dependence of PSF on neutron energy for 4, 7.5 and 14 MeV neutrons.

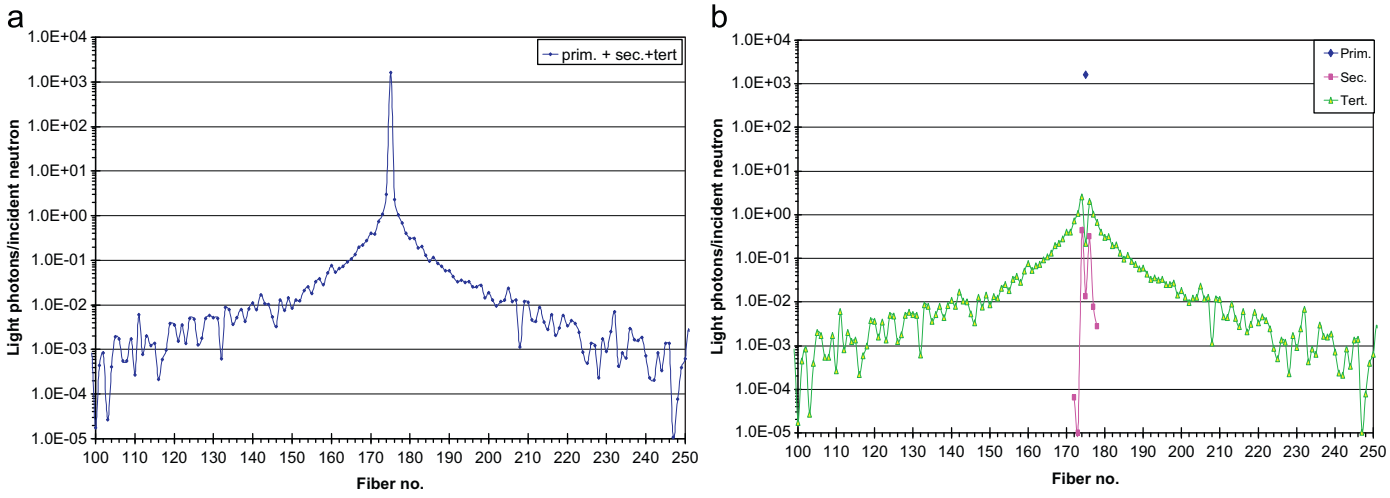

Fig. 8. (a) neutron induced total PSF and (b) contribution of each component to the total PSF.

measurement. The images in Fig. 11a, b and c (having the same gray-level scale stretching) are due to primary, secondary and tertiary light, respectively.

Fig. 12a and b shows a horizontal profile taken through the center row of the simulated image with and without (full-transmission (flat) image) the steel plate, respectively. All contributions were normalized to the primary signal of the flat image. As can be observed, only the primary signal shows the expected 7.5 MeV neutron transmission of 0.41 through the 30 mm steel plate. The contribution of the tertiary signal to the total one is quite significant in both images.

Fig. 13 shows a profile of total light (all contributors) of the 30 mm thick steel plate radiograph normalized to the total light of flat radiograph (without the object).

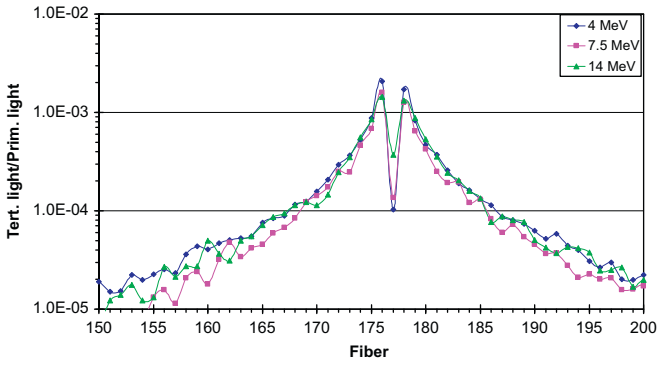

Fig. 10. Variation of normalized tertiary PSF with neutron energy.

As expected, some contrast is lost due to the processes taking place in the scintillating screen, primarily due to the relatively high contribution of the tertiary signal.

In summary, the above leads to the conclusion that the processes that take place within the screen will mainly affect image contrast, and have small influence on the spatial-resolution.

3.2. *Influence of optical and electro-optical components on spatial-resolution*

In order to examine experimentally the performance of the optical chain of the TRION Gen. 1 imaging system, (i.e. excluding neutron influence), a CTF mask (Fig. 3a) was illuminated by a uniform light source consisting of an electro-luminescent flat screen coupled to a polyethylene light diffuser. This assembly was positioned in place of the fiber scintillator screen.

First we have taken an image of the mask using only the optical components of the system, i.e., just the lenses and the CCD camera with the image-intensifier (I-I) removed. This required repositioning of the CCD camera and its I-I relay lens, such that the relay lens is focused on the virtual image created by the 120 mm F#0.95 lens. In the following measurement, the 40 mm gated I-I was introduced and the relay lens was focused on the image created on the fluorescent phosphor screen of the image-intensifier.

Fig. 14a and b shows images taken without and with image-intensifier, respectively. In both experiments the amount of photons emitted from the lamp was such that the signal was

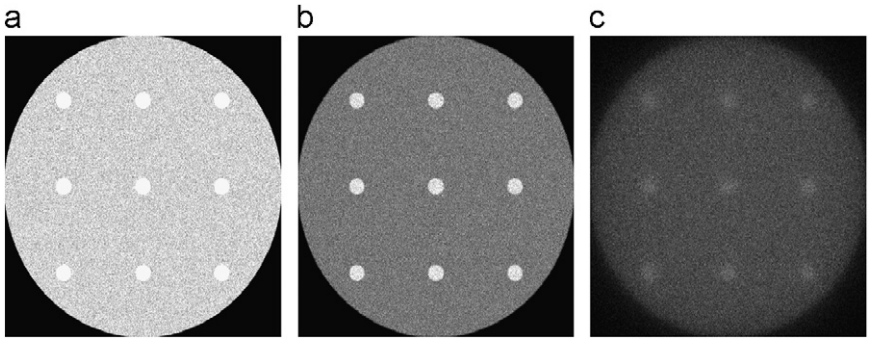

Fig. 11. GEANT calculated neutron images of a steel mask using 7.5 MeV neutrons using different light components. (a) Obtained with the primary light only, (b) with the secondary and (c) with the tertiary light only.

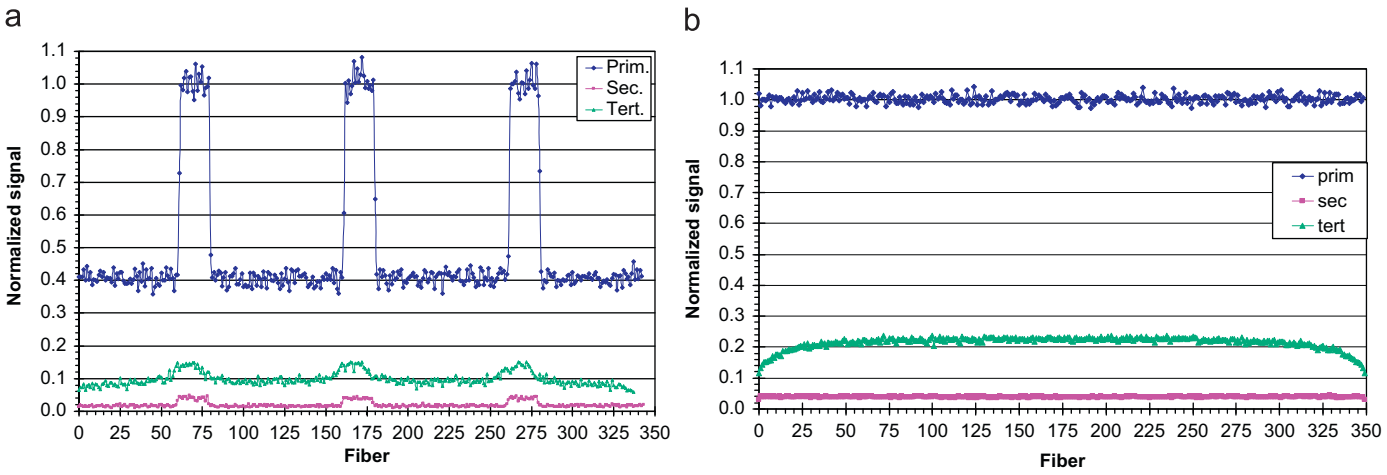

Fig. 12. Profiles from simulated images of primary, secondary and tertiary light (a) with 30 mm steel plate and (b) without it.

much higher than the I-I and CCD noises. For comparison, Fig. 14c shows the performance of the full system by presenting a neutron transmission image (7.5 MeV neutron energy) of the steel mask (seen in Fig. 3) using the 10 mm-thick fiber screen. The CTF was calculated for each image using data extracted from image profiles.

Visual inspection of the images leads to the conclusion that the image taken **without** the image-intensifier is superior. This conclusion is supported by the CTF plots, shown in Fig. 15.

Clearly, the image-intensifier significantly degrades the spatial-resolution. The manufacturer of the I-I quotes the CTF at 5 lp/mm to be ca 75% [31], which translates to 1 lp/mm at the object plane (with a de-magnification factor of 5). At present this high degradation of CTF by the I-I is not yet explained.

The neutron induced image and its CTF are clearly inferior to those obtained with the optical image of the mask. This is due to the fact that the screen adds fiber granularity and loss of contrast due to effects described in Section 3.1.2. However with 0.25×0.25 mm^2 fibers the 1 mm slits are still visible.

3.3. Experimental determination of overall PSF in TRION Gen. 2

In TRION Gen. 2, the optical chain is considerably more complex than that of Trion Gen. 1. For TRION Gen. 2 we did not perform the same detailed evaluation of the performance of the different components of the system. Only integral PSF and CTF were experimentally determined, i.e., the combined effects of neutronics, screen and optical chain.

Here we want to focus on the possibility to recover the lost contrast and spatial-resolution of the image by determining experimentally the system PSF and to use it to deconvolve it from the neutron image. The PSF determined in Section 3.1.2 was due to neutron interaction in the scintillation screen only. The overall PSF we used was determined by taking a neutron image of a relatively large well-determined aperture allowing the extraction of the PSF function by deconvolution [32].

Fig. 16b shows the radiographic transmission image of the steel plate seen on Fig. 16a (30 mm-thick with 9 holes, each 1 cm in diameter) taken with TRION Gen 2. The energy of neutrons is 7.5 MeV. Since the dimensions of the aperture are known the spatial PSF of the system was determined from this image.

Fig. 17 shows a one-dimensional profile of the PSF. The Full Width Half Maximum (FWHM) of the PSF is 7.16 fibers, which corresponds to 4 mm. This compares unfavorably to the FWHM of neutronic PSF of 1 fiber (see Fig. 8a), indicating that the loss of spatial-resolution can be mainly attributed to the optical and electro-optical components in TRION.

Fig. 18 (pink squares) shows an experimental CTF obtained using a tungsten CTF mask similar to the one described in Section 3. The CTF of TRION Gen. 2 is worse than that of TRION Gen. 1. This is due to coarser pixalization of the CCD camera and additional optical and electro-optical elements added to the chain. Fig. 16 (blue circles) shows the CTF after the Lucy–Richardson deconvolution procedure using the experimentally determined PSF (whose profile is seen in Fig. 17). Following deconvolution, the contrast shows significant improvement, especially at low spatial frequencies, however, at the expense of increased noise.

4. Summary and conclusions

Each of TRION's components may influence the contrast transfer function of the detector. The paper describes the main

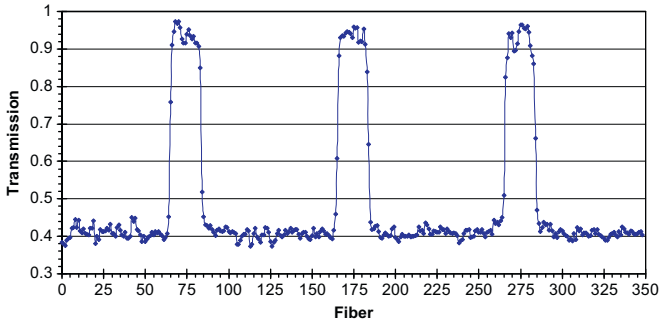

Fig. 13. Transmission profile due to 30 mm-thick steel plate showing loss of contrast due to processes in the scintillating screen.

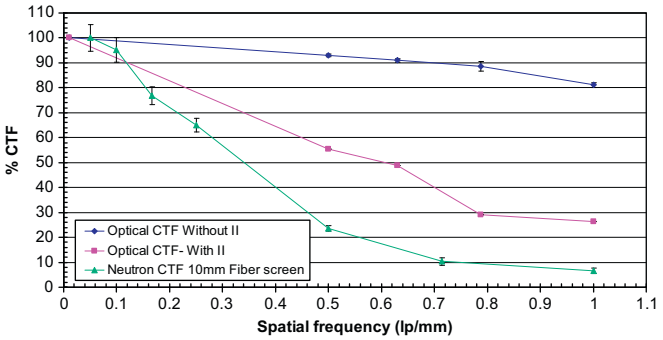

Fig. 15. CTF comparison between images taken without image-intensifier, with image-intensifier and for neutron image (7.5 MeV) containing the whole optical chain.

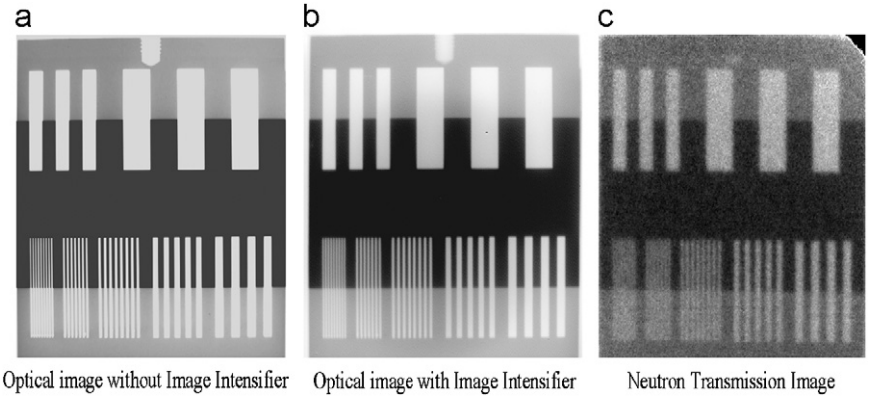

Fig. 14. (a) Light image taken without I-I, (b) with the I-I and (c) 7.5 MeV neutron image using the 10 mm-thick fiber screen.

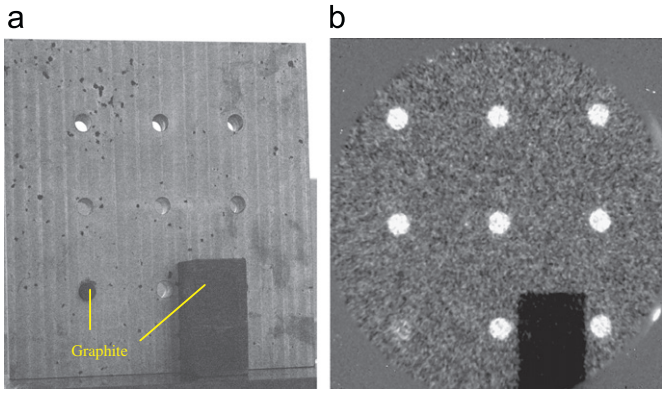

Fig. 16. (a) An actual image of the 30 mm-thick steel plate, (b) transmission image of 7.5 MeV neutrons through the steel plate

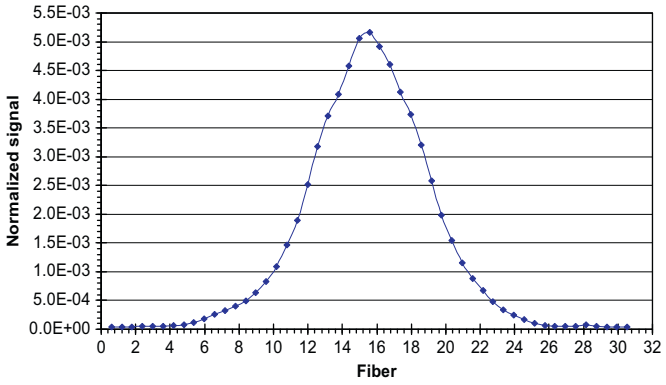

Fig. 17. Experimentally determined PSF.

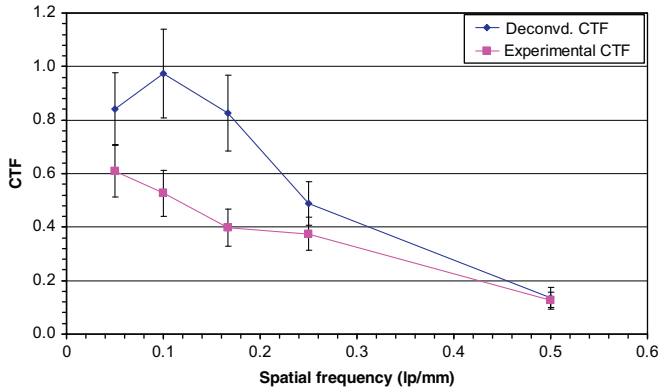

Fig. 18. Experimental CTF before and after deconvolution.

intrinsic contributions to image quality due to the type and geometry of scintillating screen, neutron scattering and proton energy deposition within the screen and spatial-resolution degradation introduced by the optical and electro-optical components.

Apart from the effects of the "neutronics" the image-intensifier introduces the most significant image degradation. The optical and electro-optical components are the main contributors to spatial-resolution degradation in TRION Gen. 2.

As expected, the spatial-resolution obtained by the fiber scintillator screen exceeds the one displayed by a regular slab scintillator due the latter's dependence on the depth-of-field effect. This allows usage of fiber scintillator screens of larger thickness, which translates to higher detection efficiency. An unwanted side-effect of thickness enlargement is enhanced neutron scatter within the scintillator screen, which is the main reason for loss of contrast. Nevertheless, deconvolution of experimental image that contains all of the above degrading factors restored significantly the contrast and the spatial-resolution of the fast neutron image.

References

[1] H. Strecker, G. Harding, H. Bomsdorf, J. Kanzenbach, R. Linde, G. Martens, Detection of explosives in airport baggage using coherent X-ray scatter, in: Proceedings of the SPIE, Austria, 1993.
[2] J.C. Overley, Nucl. Instr. and Meth. B 24/25 (1987) 1058.
[3] J.C. Overley, Int. J. Appl. Radiat. 36 (3) (1985) 185.
[4] National Materials Advisory-Board (NMAB), The Practicality of Pulsed Fast Neutron Transmission Spectroscopy for Aviation Security, National Academy Press, Washington D.C., 1999, p. 20418.
[5] J.E. Eberhardt, S. Rainey, R.J. Stevens, B.D. Sowerby, J.R. Tickner, Appl. Radiat. Isot. 63 (2) (2005) 179.
[6] G. Chen, R.C. Lanza, IEEE Trans. Nucl. Sci. NS-49 (4) (2002) 1919.
[7] A. Buffler, Radiat. Phys. Chem. 71 (2004) 853.
[8] A. Buffler, J. Tickner, Detecting contraband using neutrons: challenges and future directions, Radiat. Meas., in press, corrected proof, 〈http://dx.doi.org/10.1016/j.radmeas.2010.06.010〉.
[9] T. Gozani, Nucl. Instr. and Meth. A 353 (1994) 635.
[10] D. Strellis, T. Gozani, J. Stevenson, Air cargo inspection using Pulsed Fast Neutron Analysis, in: Proceedings of the IAEA Conference on Neutron Based Techniques for the Detection of Illicit Materials and Explosives, Vienna, 4–8 May 2009, SM/EN-05.
[11] B.D. Sowerby, N.G. Cutmore, Y. Liu, H. Peng, J. Tickner, Y. Xie, C. Zong, Recent developments in fast neutron radiography for the interrogation of air cargo containers, in: Proceedings of IAEA Conference on Neutron Based Techniques for the Detection of Illicit Materials and Explosives, Vienna, 4–8 May 2009, SM/EN-01.
[12] Z. Yubin, G. Zhiyu, T. Guoyou, M. Dawei, Eng. Sci. 7 (4) (2009) 83.
[13] D. Vartsky, Prospects of fast-neutron resonance radiography and requirements for instrumentation, in: Proceedings of the International Workshop on Fast Neutron Detectors and Applications, POS(FNDA2006)084, 2006, 〈http://pos.sissa.it//archive/conferences/025/008/〉.
[14] G.E. Sieger, Use of simulated suitcases in refining explosive detection algorithms, 1996; 〈http://www.uoregon.edu/~lefevre/ges.html〉.
[15] J.C. Overley, M.S. Chmelik, R.J. Rasmussen, G.E. Sieger, H.W. Lefevre, Results of Blind Tests for Explosives in Luggage Using Fast-Neutron Transmission Spectroscopy (FNTS), 1996, 〈http://darkwing.uoregon.edu/~lefevre/faa talk1.html〉.
[16] J.C. Overley, Nucl. Instr. and Meth. B 99 (1995) 728.
[17] J.C. Overley, M.S. Chmelik, R.J. Rasmussen, R.M.S. Schofield, G.E. Sieger, H.W. Lefevre, Nucl. Instr. and Meth. B 251 (2006) 470–478.
[18] H.W. Lefevre, M.S. Chmelik, R.J. Rasmussen, R.M.S. Schofield, G.E. Sieger, J.C. Overley, Proc. SPIE 2867 (1997) 206.
[19] T.G. Miller, Proc. SPIE 2093 (1994) 204.
[20] T.G. Miller, Proc. SPIE 2276 (1994) 200.
[21] T.G. Miller, R.A. Krauss, Proc. SPIE 2511 (1995) 14.
[22] T.G. Miller, P.K. Van Staagen, B.C. Gibson, J.L. Orthel, R.A. Krauss, Proc. SPIE 2936 (1997) 102.
[23] Tensor-Technology, Multi-dimensional neutron radiometer ("MDNR"), personal communication, 2005.
[24] V. Dangendorf, C. Kersten, G. Laczko, D. Vartsky, I. Mor, M.B. Goldberg, G. Feldman, A. Breskin, R. Chechik, O. Jagutzky, U. Spillman, Nucl. Instr. and Meth. A 535 (2004) 93.
[25] I. Mor, D. Vartsky, D. Bar, G. Feldman, M.B. Goldberg, D. Katz, E. Sayag, I. Shmueli, Y. Cohen, A. Tal, Z. Vagish, B. Bromberger, V. Dangendorf, D. Mugai, K. Tittelmeier, M. Weierganz, J. Instr. JINST 4 (2009) P05016.
[26] D. Vartsky, G. Feldman, I. Mor, M.B. Goldberg, D. Bar, V. Dangendorf, J. Instr. 4 (2009) P02001.
[27] I. Mor, Energy resolved fast neutron imaging via time resolved optical readout, M.Sc. Thesis, 2006, 〈http://jinst.sissa.it/theses/2006_JINST_TH_002.jsp〉.
[28] Saint-Gobain crystals and detectors, Scintillating optical fibers, 〈http://www.detectors.saint-gobain.com/uploadedFiles/SGdetectors/Documents/Brochures/Scintillating-Optical-Fibers-Brochure.pdf〉.
[29] J.F. Janni, At. Data Nucl. Data Tables 27 (1982) 304.
[30] GEANT 3.21, detector description and simulation tool, CERN program library long writeupW5013, CERN, Geneva, 1993, 〈http://wwwasdoc.web.cern.ch/wwwasdoc/geant_html3/geantall.html〉.
[31] Photek LTD., MCP image intensifiers, 〈http://www.photek.com/datasheets/Image%20Intensifiers.pdf〉.
[32] F. Grunauer, Nucl. Inst. and Meth. A 566 (2006) 654.